Chemical Engineering Journal 413 (2021) 127387

Contents lists available at ScienceDirect

Chemical Engineering Journal

journal homepage: www.elsevier.com/locate/cej

A synchronous defect passivation strategy for constructing high-performance and stable planar perovskite solar cells

Yansen Sun [a,b], Zhenyu Pang [a,b], Yingnan Quan [c], Donglai Han [d], Xinyuan Zhang [a,b], Xin Ge [c], Fengyou Wang [c], Yunfei Sun [c], Jinghai Yang [c,*], Lili Yang [c,*]

[a] Changchun Institute of Optics, Fine Mechanics and Physics, Chinese Academy of Sciences, Changchun 130033, PR China
[b] University of Chinese Academy of Sciences, Beijing 100049, PR China
[c] Key Laboratory of Functional Materials Physics and Chemistry of the Ministry of Education, Jilin Normal University, Changchun 130103, PR China
[d] School of Materials Science and Engineering, Changchun University of Science and Technology, Changchun 130022, PR China

ARTICLE INFO

Keywords:
Perovskite solar cells
Defect passivation
Alkali metal ions
Power conversion efficiency

ABSTRACT

The diverse defects within perovskite film, electron transport layer (ETL) and their interface greatly impair the power conversion efficiency (PCE), hysteresis and stability of perovskite solar cells (PSCs). Herein, we propose a synchronous defect passivation strategy by introducing chelating agent containing movable alkali metal cations, i.e. sodium tartrate (STA)/potassium sodium tartrate (PSTA) into SnO_2 aqueous colloidal dispersions to realize the efficient regulation of ETL, perovskite layer and their interface properties. That is, the chelating function and existence of alkali metal ions in additives lead to uniform, less defective and highly conductive SnO_2 ETLs, which provides outstanding platforms for depositing perovskite films with high-quality crystallinity to improve the interfacial charge transfer. In particular, **a** part of Na^+ and K^+ ions of additives can enter into perovskite film through thermal diffusion and passivate the defects by coordinating with under-coordinated halides via ionic interactions or electrostatic adsorption on the negative charged defects at surface and grain boundaries. Such synchronous optimization for ETLs, perovskite and their interface enables the realization of high PCEs of 20.38% and 21.14% with reduced hysteresis and improved stability for STA-SnO_2 and PSTA-SnO_2 based PSCs, respectively. This work greatly simplifies the defect passivation process and provides a promising low-cost technique for large-scale manufacturing efficient and stable planar PSCs.

1. Introduction

Perovskite solar cells (PSCs) are undergoing an unprecedented development stage due to the excellent photoelectric properties of perovskite polycrystalline materials. Currently, the power conversion efficiency (PCE) of the state-of-the-art PSCs has soared to 25.2% [1,2]. Such rapid progress greatly depends on the optimization of perovskite layer, charge transport layer and their interface properties [3–5]. Moreover, the emergence of new charge transport materials, the optimized design of device structure as well as the usage of different conductive substrates continuously promotes the diversification of devices [6,7]. Nevertheless, the generation of various defects during the preparation of PSCs still seems inevitable. Generally, defects can serve as recombination centers at ETL, perovskite film surface, grain boundaries and their interface to capture photo-generated charge carriers, leading to poor charge transport and severe non-radiative recombination losses in PSCs [8–10]. Therefore, the elimination or passivation of those defects holds great promise for the further development of PSCs especially in the PCE, current density–voltage (J-V) hysteresis and device stability.

For n-i-p planar PSCs, electron transport layer (ETL) usually plays the main and critical role in achieving high-performance of devices. Apart from acting the role in extracting the electrons and blocking the holes, it can also affect the crystal growth dynamics process of perovskite polycrystalline films, especially for the heterogeneous nucleation period of perovskite grains [11,12]. Meanwhile, the technical maneuverability also makes it a research hotspot since the enhancement of device performance can be achieved by optimizing ETLs themselves or their surface properties. Currently, SnO_2 acted as a promising material has aroused extensive research interest since You's team first obtained the high-performance planar PSCs on SnO_2 ETL prepared by a simple spin-coating method with a relatively low annealing temperature of 150 °C using commercial SnO_2 aqueous colloidal dispersions [13]. However,

* Corresponding authors.
E-mail addresses: jhyang1@jlnu.edu.cn (J. Yang), llyang1980@126.com (L. Yang).

https://doi.org/10.1016/j.cej.2020.127387
Received 27 June 2020; Received in revised form 30 September 2020; Accepted 13 October 2020
Available online 18 October 2020

considering the drawbacks of such low-temperature spin-coating method and the agglomerative nature of SnO_2 nanoparticles themselves in colloidal dispersions, it is inevitable that these SnO_2 thin films will have numerous defects and pin-holes, deteriorating the film surface conditions of the films and increasing the recombination of photo-generated charge carriers [14]. Even worse, the poor quality of SnO_2 thin film will also have a malignant effect on the nucleation dynamics process of perovskite polycrystalline films and their interface property. As a result, the above chain effects will eventually lead to problems such as reduced PCE, severe hysteresis behavior, inferior stability of PSCs and poor device reproducibility [15].

With regard to these problems, interface modification has been considered as an effective method to suppress the non-radiative recombination at the interface, adjust the energy level structure, reduce the open-circuit voltage (Voc) losses and enhance the charge transfer efficiencies [16–18]. To date, a variety of modified materials and passivation methods have been developed to boost the device performance and stability, such as adopting self-assembled monolayers, ultra-thin organic polymers and double ETLs [19–21]. Nevertheless, the aforementioned methods not only complicate the device fabrication process but also fail to fundamentally address the film quality problem, such as effectively reducing the formation of oxygen vacancy induced non-radiative recombination centers in SnO_2 ETL [22]. In fact, the addition of functional additives to the SnO_2 aqueous colloidal dispersions makes it easy to prepare homogeneous, dense SnO_2 films with improved photoelectric properties. On this basis, Liu's group found that using an appropriate amount of chelating agent ethylenediaminetetraacetic acid (EDTA) in the dispersions to complex SnO_2 nanoparticles can yield high-quality SnO_2 films with improved electron mobility, enhanced optical transmittance and reduced work function since the oxygen atoms on the carboxyl group can be combined with Sn^{4+} in SnO_2 nanoparticles in the form of coordination bonds to form a complex, which can suppress the non-radiative recombination and improve the electron transfer and extraction efficiency at the ETL and interface [23]. Although it has been reported the introduction of chelating additives to modulate SnO_2 ETLs indeed suppress the defects and reduce the number of pinholes in ETLs to induce the formation of better perovskite films, it does not synchronously passivate the ionic defects, shallow or deep level defects such as MA^+ vacancies [24], PbI_3^- anti-site defects [25], under-coordinated Pb^{2+} ions and halide ions (I^-) at the surface/grain boundaries of perovskite films [26–28], which will limit the further enhancement of PCE and worsen the stability for PSCs if nothing else is done.

In general, defects in perovskite films can be passivated by forming coordination bonds, ionic bonds, Lewis acid/base adducts or by introducing free metal ions, etc [29]. Wherein, the usage of metal ions seems to be one of the most effective methods, and it has also been shown that the formation of ionic bonds and electrostatic interactions between metal ions and under-coordinated halides can effectively suppress the ion migration within devices [30]. Therefore, if a chelating agent containing free metal ions is selected and introduced into the fabrication process of SnO_2 ETL, it is expected that the properties of the ETL, perovskite absorber layer and their interface will be synchronously regulated considering the free metal ions can diffuse from ETL to perovskite surface and grain boundaries during the annealing process of preparing perovskite films. That is, an amazing photovoltaic (PV) performance should be obtained with enhanced stability and inhibited hysteresis.

Accordingly, three chelating agents such as tartaric acid (TA), sodium tartrate (STA) and potassium sodium tartrate (PSTA) are selected as additives to be introduced into SnO_2 aqueous colloidal dispersions, and the corresponding chemical structures are shown in Fig. 1, respectively. The role and effects of these chelating agents with or without (w or w/o) alkali metal cations on improving the PV performance of PSCs are explored for the first time. The introduction of STA and PSTA additives to modulate SnO_2 ETLs has successfully brought some novel

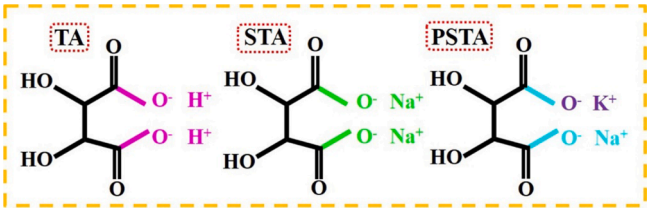

Fig. 1. The chemical structure of the chelating agent (a) TA, (b) STA and (c) PSTA.

cascading effects on SnO_2 ETL, perovskite film and interface properties of devices. Both ETLs and perovskite films exhibit better crystallinity, reduced defect densities and improved charge transport properties. The chelating mechanism can be summarized as follows: according to the Lewis acid-base theory, a coordinate bond can be formed between the electron pair acceptor and the electron pair donor. Wherein, Sn^{4+} can accept the electrons due to the presence of empty orbitals in their energy-level structure, and the oxygen atoms on the carboxyl groups in the additive can provide the electrons due to the presence of lone pair electrons, so that they can form complexes through the coordinate bonding [31]. Moreover, the alkali metal cations in STA and PSTA indeed diffuse into the perovskite films to suppress the defect states and modify the interface properties, further boosting the PV performance of PSCs. Moreover, the form of alkali metal-only thermal diffusion reveals the passivation effect of K^+ and Na^+ on perovskite film more visually than the introduction of salts containing alkali metals into the perovskite precursor solutions. The highest PCEs of 21.14% and 20.38% have been achieved for devices based on PSTA-SnO_2 and STA-SnO_2 ETLs, respectively, outperforming most of $MA_xFA_{1-x}PbI_3$ PSCs based on SnO_2 ETLs. Particularly, PSCs based on PSTA-SnO_2 ETL also exhibit excellent performance with negligible hysteresis, enhanced stability and higher repeatability. In short, we have adopted an effective and simple method to simultaneously regulate the photoelectric properties of ETL, improve the quality of the perovskite layer and interface properties, which plays a guiding role in simultaneously enhancing the PV performance and stability of PSCs.

2. Experimental section

2.1. Materials

Chemicals like lead iodide (PbI_2, 99.9%), formamidinium iodide (FAI, ≥99.5%), methylammonium iodide (MAI, ≥99.5%), 2,2′,7,7′-tetrakis(N,N-di-p-methoxyphenylamine)-9,9-spirobifluorene (Spiro-OMeTAD), Bis(trifluoromethane) sulfonimide lithium salt (Li-TFSI, 99.9%), solvents including N,N-dimethylformamide (DMF, >99.9%), dimethyl sulfoxide (DMSO, >99.9%), 4-*tert*-butylpyridine (TBP, 99%) and chlorobenzene (CB, >99.5%) were purchased from Yingkou Youxuan Trade Co., Ltd. The SnO_2 aqueous colloidal precursor (tin (IV) oxide, 15% in H_2O colloidal dispersion) was ordered from Alfa Aesar. Tartaric acid (TA, >99.5%), sodium tartrate (STA, >99.5%) and potassium sodium tartrate (PSTA, >99.5%) were obtained from Sinopharm Chemical Reagent Co., Ltd.

2.2. Preparation of devices

The glass/ITO substrates were successively cleaned with deionized (DI) water, detergent, ethanol, acetone and isopropanol under ultrasonic condition for 30 min, respectively. Hereafter, all substrates were dried in an oven at 60° for 2 h. Before usage, they were further cleaned by Ultraviolet/Ozone (UV-O_3) for 20 min to remove the surface functional groups. The pristine SnO_2 precursor solution was prepared by diluting the SnO_2 colloidal dispersion with deionized (DI) water (volume ratio of 1:1) and stirring for 3 h. Considering the different chelating abilities of

TA, STA and PSTA, we firstly optimized the concentrations of each additive to be 0.8 M, 1.5 M and 1.4 M, respectively, to guarantee their similar chelating effects in SnO_2 ETLs. Then SnO_2 colloidal dispersions with equal volumes were slowly added to these additive solutions followed with stirring for 3 h to obtain the TA-SnO_2, STA-SnO_2 and PSTA-SnO_2 precursor solutions. All these SnO_2 precursor solutions were spin-coated onto ITO substrates at 5000 rpm for 30 s and then annealed on a hotplate at 150 °C for 30 min to obtain the corresponding ETLs. Then all the above samples were transferred to the glove box after UV-O_3 treatment for 20 min.

To prepare 1.3 M of $MA_{0.85}FA_{0.15}PbI_3$-based perovskite precursor solution, FAI powder (0.034 g), MAI powder (0.176 g) and an appropriate excess amount of PbI_2 powder (0.637 g) were dissolved into the solvents of DMF (800 μL) and DMSO (200 μL). Whereafter, we spin-coated 85 μL of hybrid solution onto these ETLs in a two-step process at 500 rpm for 10 s and 4000 rpm for 30 s. During the second step, 400 μL of chlorobenzene (CB) was slowly dripped onto the substrates at 20 s before finishing the procedure. The as-prepared perovskite films were then annealed at 130 °C for 15 min. The hole transport materials was prepared by dissolving 72.3 mg of spiro-OMeTAD, 28.8 μL of TBP and 17.5 μL of Li-TFSI (520 mg Li-TFSI dissolved in 1 mL acetonitrile) in 1 mL of chlorobenzene. We extracted 65 μL of them and spin-coated on perovskite films at 3000 rpm for 30 s. Finally, a 150 nm-thickness Ag was deposited on the top as a back electrode by thermal evaporation under a high vacuum ($<6.6 \times 10^{-4}$ Pa) with the evaporation rate of 1 Å/s.

2.3. Film and device characterization

The optical absorption spectra were measured in the range of 350–850 nm using an Ultraviolet–visible-near infrared (UV–Vis-NIR) spectrophotometer (SHIMADZU UV-3101PC). The X-ray diffraction (XRD) patterns were performed by a Japan Rigaku D/max-ga X-ray diffractometer using Cu Kα radiation (λ = 1.5418 Å) at 40 kV and 200 mA under room temperature. X-ray photoelectron spectra (XPS) were conducted by the Thermo ESCALAB 250 measurement system. Ultraviolet photoemission spectra (UPS) were also obtained using this system at ultra-high vacuum pressure. The thermogravimetric and differential scanning heat measurements were conducted by NETZSCH STA 449F3 system with the temperature increasing rate of 10 °C/min under nitrogen-protected conditions. A field emission scanning electron microscope (SEM) (Hitachi S-4800 system) equipped with an energy dispersive X-ray spectroscopy (EDS) system (EDAX Genesis 2000) was utilized to obtain the top-down and cross-sectional SEM images. The Raman measurements were carried on Renishaw inVia confocal Raman microscope with 514.5 nm excitation. The steady-state photoluminescence (PL) spectra and time-resolved photoluminescence (TRPL) spectra were recorded by a spectrofluorometer (Horiba, Fluorolog-3-TCSPC) with an excitation wavelength of 405 nm. Atomic force microscope (AFM) measurements were performed by Oxford Instruments (MFP-3D-BIO) equipped with a time-resolved fluorescence confocal microscopy. The current density versus voltage (J-V) characteristic curves were measured using a Keithley 2400 source meter measurement system equipped with AM1.5G spectrum, which was calibrated by a standard silicon reference cell (91160 V Oriel Instruments) before usage to achieve the illumination of 1000 Wm^{-2}. All PSCs were measured by employing a non-reflective metal mask with an effective area of 0.1 cm^2. The forward (from 0 to 1.2 V) and reverse (from 1.2 to 0 V) scan rates were set to 80 mVs^{-1} under ambient condition with relative humidity (RH) of 45 ± 5% and temperature of 20 ± 5 °C. Long term stability tests were also conducted in ambient environment with RH of 40 ± 5% and temperature of 25 °C using the unencapsulated devices. The incident photon-to-electron conversion efficiency (IPCE) spectra were measured from 360 nm to 1000 nm using an IPCE set-up (QEX10, PV Measurement) under monochromatic light and the photocurrent was measured using a lock-in amplifier. The electrochemical impedance spectra (EIS) were tested by an electrochemical workstation (PARSTAT 4000) under dark condition at a 0 V bias voltage with an alternative signal amplitude of 5 mV and a frequency range of 1 MHz to 0.01 kHz.

3. Results and discussion

To ensure that all these additives including TA, STA and PSTA are always active in the formation process of the SnO_2 ETLs, we first performed TG/DSC measurements. All results are presented and summarized in Fig. S1, indicating that they will not be decomposed during the annealing process at 150 °C. Moreover, we also investigated the chelating abilities of the above-mentioned additives in SnO_2 aqueous colloidal dispersions and their effects on device performance to determine their optimal doping content, respectively, which are shown in Figs. S2 and S3. The detailed analyzation can be seen in our supporting information. The effects of these chelating additives on regulating the photoelectric properties of SnO_2 ETLs were subsequently explored. Fig. 2a presents the optical transmission spectra of SnO_2, TA-SnO_2, STA-SnO_2 and PSTA-SnO_2 films deposited on ITO. All additive-modulated and the control SnO_2 ETLs exhibited higher transmittance over the entire spectral range, ensuring that more light can be utilized by perovskite films. The dark current density–voltage (J-V) and Tafel measurements conducted with device structure of ITO/ETLs/Ag were shown in Fig. 2b. Along with the introduction of TA, STA and PSTA, the electrical conductivity of these SnO_2 ETLs gradually increased from 6.87×10^{-4} to 7.41×10^{-4}, 7.89×10^{-4} and 8.53×10^{-4} mS cm^{-1}. To explore the reasons, the corresponding SnO_2 films were prepared on smooth silicon wafers using the same preparation procedure. As shown in the corresponding top-view scanning electron microscopy (SEM) images in Fig. S4a–d, the average size of the SnO_2 nanocrystals for all films are similar, all in the range of 20–30 nm. However, the distribution of recrystallized SnO_2 nanocrystals gradually turns homogeneous and dense as introducing TA, STA and PSTA, respectively, indicating the chelating agents can ameliorate the agglomerative nature of SnO_2 nanoparticles in colloidal dispersions, and the differences among them can be attributed to differences in chelating capacity. In addition, the energy dispersive X-ray spectra (EDS) and mapping images presented in Fig. S4e–h and S4i-n reveal the existence of Na, K, Sn and O elements in corresponding SnO_2 films.

The X-ray photoelectron spectroscopies (XPS) are further employed to demonstrate the chelation between additives of TA, STA, PSTA and Sn^{4+}, as well as the existence of Na^+ and K^+ ions in STA-SnO_2 and PSTA-SnO_2 ETLs. As shown in Fig. 2c, some extra peaks located at 1072, 377.6, 295.7 and 292.7 eV were found in the XPS survey spectra of the STA-SnO_2 and PSTA-SnO_2 films, which can be attributed to the presence of Na 1 s, K 2 s, K $2p^{1/2}$ and K $2p^{3/2}$ respectively, exhibiting a better agreement with the EDS and mapping results. The detailed information of the binding energies for these elements was shown in Fig. S5. The $Sn3d_{3/2}$ and $Sn3d_{5/2}$ core-level lines for all SnO_2 films located around 494.9 eV and 486.4 eV are presented in Fig. 2d. The specific values of the corresponding $Sn3d_{5/2}$ binding energies are summarized in Fig. 2e. Obviously, the Sn 3d peaks in modulated SnO_2 ETLs shift to higher binding energy compared to that of control SnO_2 film. We further fitted the Sn 3d XPS curves with Gaussian–Lorentzian functions due to its asymmetric shape (Fig. S6) proving the co-existence of Sn^{4+}, Sn^{2+} and Sn in these SnO2 thin films [32,33]. To justify whether the ratio variation among three species caused the shift of binding energy, we summarized the relative ratio of Sn^{4+}/Sn^{2+} in Table S1 and obtained the nearly same values for all SnO_2 samples. Thus, there is must some other factor to cause the peak shift. Since the additives bring lots of oxygen-containing groups into SnO_2 aqueous colloidal dispersions, we then provided the core-level lines of O 1s of these SnO_2 samples (Fig. S6) and performed the Gaussian–Lorentzian fitting as well. The lattice oxygens of O^{Sn4+} and O^{Sn2+}, the oxygen in –OH and oxygen vacancy coexisted in the control SnO_2 sample. While, beside these three oxygen species, another oxygen specie in –COO– groups located at 532.2 eV appeared in

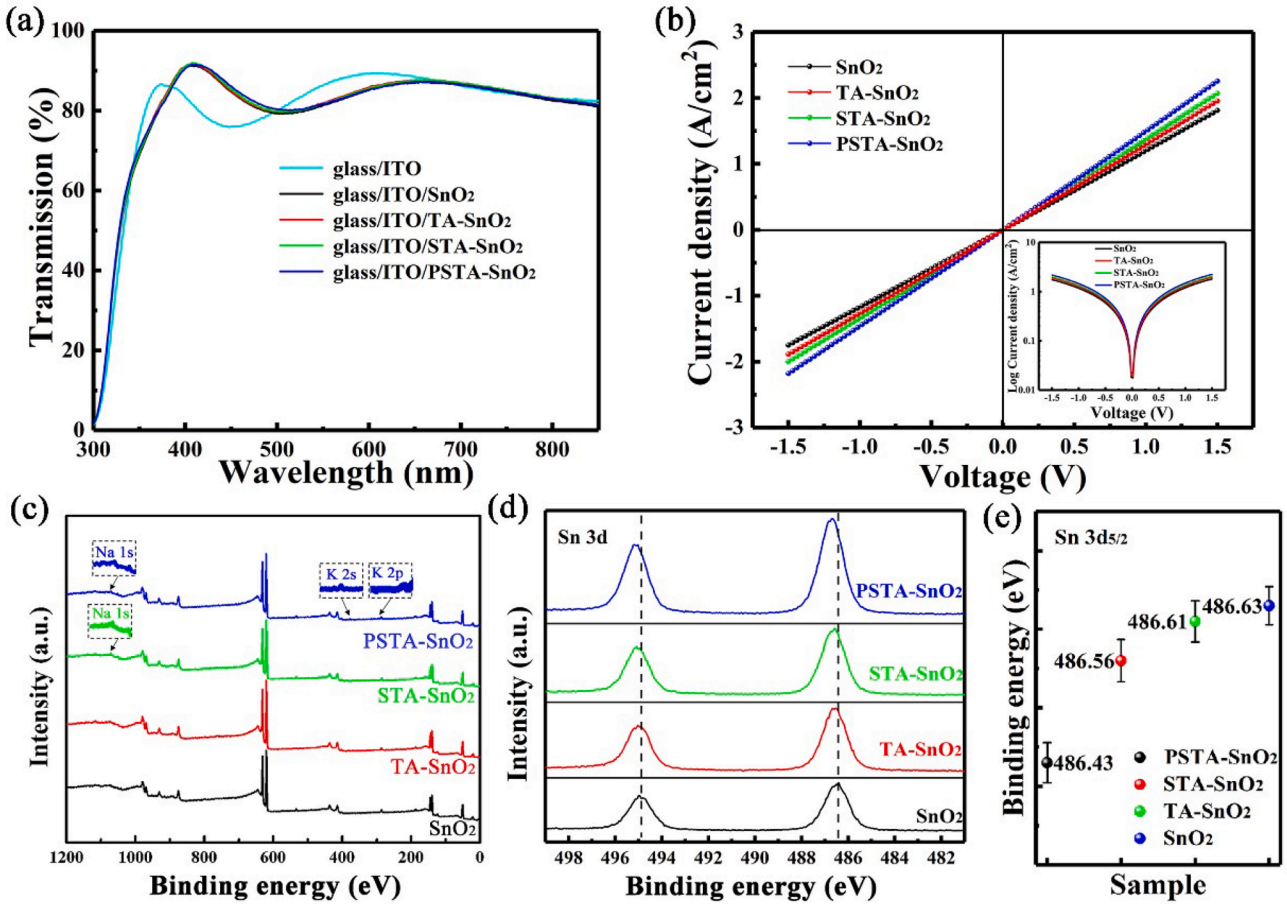

Fig. 2. (a) Optical transmission spectra of SnO_2, TA-SnO_2, STA-SnO_2 and PSTA-SnO_2 films deposited on ITO. (b) The J–V curves for electron only devices with inset of Tafel plots. (c) The XPS survey spectra of SnO_2, TA-SnO_2, STA-SnO_2 and PSTA-SnO_2 films. (d) High-resolution XPS spectra of Sn3d. (e) The specific binding energy of $Sn3d_{5/2}$ for SnO_2, TA-SnO_2, STA-SnO_2 and PSTA-SnO_2 films.

additive-modified SnO_2 samples due to the existence of –COOH in TA, STA and PSTA. Meanwhile, the peak position and content ratio of –COO– in TA-, STA- and PSTA-SnO_2 films are 532.22 eV (10.28%), 532.14 eV (11.44%) and 532.12 eV (13.21%), respectively. All these results indicated some reactions such as chelating might happen between Sn ions and –COOH. In detail, the O atoms in carboxyl groups contain two lone-pair electrons and own strong electronegativity, which is beneficial for them to chemically bound with Sn^{4+} ions. Thus, the shared electron cloud density of the tin element and the oxygen element in SnO_2 films is closer to the oxygen element and farther away from the Sn element, which finally results in the peak shift of Sn 3d core level lines [34,35].

Such proved chelating effects between these additives and under-coordinated Sn^{4+} will help to reduce the pin-holes and intrinsic defects such as oxygen vacancies in SnO_2 crystal. To further validate the variation of SnO_2 nanocrystal oxygen defects caused by additives, we then conducted the Raman measurements on SnO_2 and TA-, STA- and PSTA-based SnO_2 samples since Raman spectroscopy is an important analytical method applied to the study of molecular structure [36]. As shown in Fig. S7, a broad, asymmetric and strong Raman peak appeared for all samples. After Gaussian-Lorentzian fitting on the curves, the Raman peaks at 483, 623 and 754 cm^{-1} can be assigned to the E_g, A_{1g} and B_{2g} vibration modes, respectively [37]. Another two peaks at 540 and 676 cm^{-1} arise from the disorder during the activation of SnO_2 nanocrystals and the surface phonon modes [38]. All these characteristic peaks indicate the tetragonal rutile structure and nanocrystalline nature of the SnO_2 nanoparticles. Besides these, a broad and strong Raman peak at 573 cm^{-1} can be found for all samples, which is related to oxygen vacancies of SnO_2 nanocrystal. The corresponding percentages of each peak area are shown in Table S3, the gradually reduced contents means the reduced oxygen vacancies [39,40]. Therefore, the introduction of additives not only optimizes the ETLs with improved crystal quality, uniform morphologies and enhanced photoelectric properties, but also supplies a desired platform for depositing high-quality perovskite films [41,42].

To further investigate the benign effects of the modified ETLs on perovskite films, Fig. 3a-d shows the top-view scanning electron microscopy (SEM) images of $MA_{0.85}FA_{0.15}PbI_3$ films deposited on SnO_2, TA-SnO_2, STA-SnO_2 and PSTA-SnO_2 ETLs. Except for a few of pinholes appearing on the SnO_2-based perovskite film, all other perovskite films contain continuous and regular perovskite crystal grains. None of the pinholes in perovskite films deposited on the additive-modulated ETLs can be attributed to the improved quality of SnO_2 ETLs. The corresponding grain size distributions are summarized in Fig. S8, where PSTA-SnO_2 based one shows the largest average grain size of ~700 nm among them. The cross-sectional SEM image of SnO_2/perovskite presented in Fig. S9 exhibits richest and messy grain boundaries, and some cracks are also found at ETL/perovskite interface. In contrast, the PSTA-SnO_2/perovskite sample not only exhibits well-crystallized grain morphology, but also owns the largest average grain size, which can be ascribed to the reduction of surface energy and the optimization of flatness in those modified ETLs [43]. Subsequently, we further recorded corresponding atomic force microscopy (AFM) images to analyze the topography changes in $MA_{0.85}FA_{0.15}PbI_3$ films deposited on different SnO_2 ETLs. As shown in Fig. 3e-h, the root-mean-square (RMS) roughness of PSTA-SnO_2/perovskite is only 10.9 nm, which is much smaller

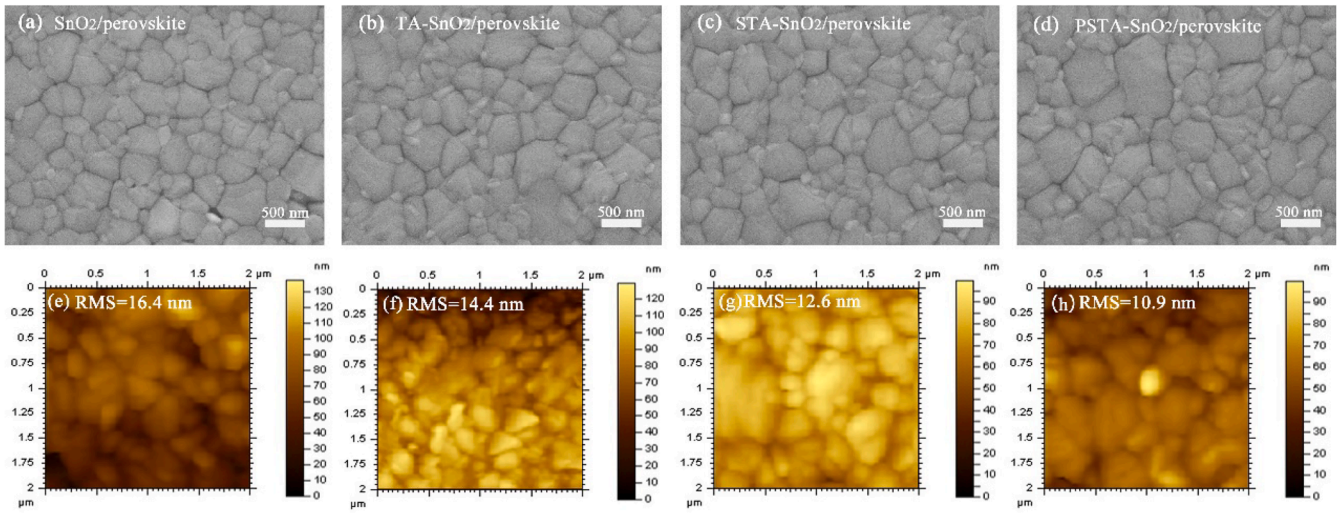

Fig. 3. SEM images of $MA_{0.85}FA_{0.15}PbI_3$ films deposited on (a) SnO_2, (b) TA-SnO_2, (c) STA-SnO_2, (d) PSTA-SnO_2 ETLs. AFM images of $MA_{0.85}FA_{0.15}PbI_3$ films spin-coated on (e) SnO_2, (f) TA-SnO_2, (g) STA-SnO_2, (h) PSTA-SnO_2 ETLs.

than that of perovskite films deposited on STA-SnO_2 (12.6 nm), TA-SnO_2 (14.4 nm) and SnO_2 (16.4 nm), further demonstrating the formation of smoother and flatter perovskite films.

Considering the existing theory of crystal nucleation and growth [44], the heterogeneous nucleation process is closely related to the Gibbs free energy ΔG,

$$\Delta G_{heterogeneous} = \Delta G_{homogeneous} f(\theta)$$

where $f(\theta)=(2-3\cos\theta+\cos^3\theta)/4$ and θ is the contact angle of perovskite precursor on these ETLs [45]. The smaller value of θ will lead to a reduction in $\Delta G_{\text{heterogeneous}}$, thus promoting nucleation process. The contact angles of perovskite precursor on the SnO_2, TA-SnO_2, STA-SnO_2 and PSTA-SnO_2 films shown in Fig. S10 gradually decrease, which helps to increase the crystal nucleation density, promote the growth process of perovskite films, and eventually achieve more homogeneous films with larger grain size. The X-ray diffraction (XRD) patterns in Fig. S11 indicate all perovskite films own cubic structure. And better crystallinities have been obtained for the perovskite films grown on additive-modulated SnO_2 ETLs due to the stronger diffraction peak intensities. Moreover, a small diffraction peak located at 12.65° appears in all XRD patterns, indicating the existence of unreacted PbI_2 [46]. According to previous reports, moderate amounts of residual PbI_2 are beneficial for enhancing device performance since they can passivate the defects on surface and at grain boundaries of perovskite films [47]. All above

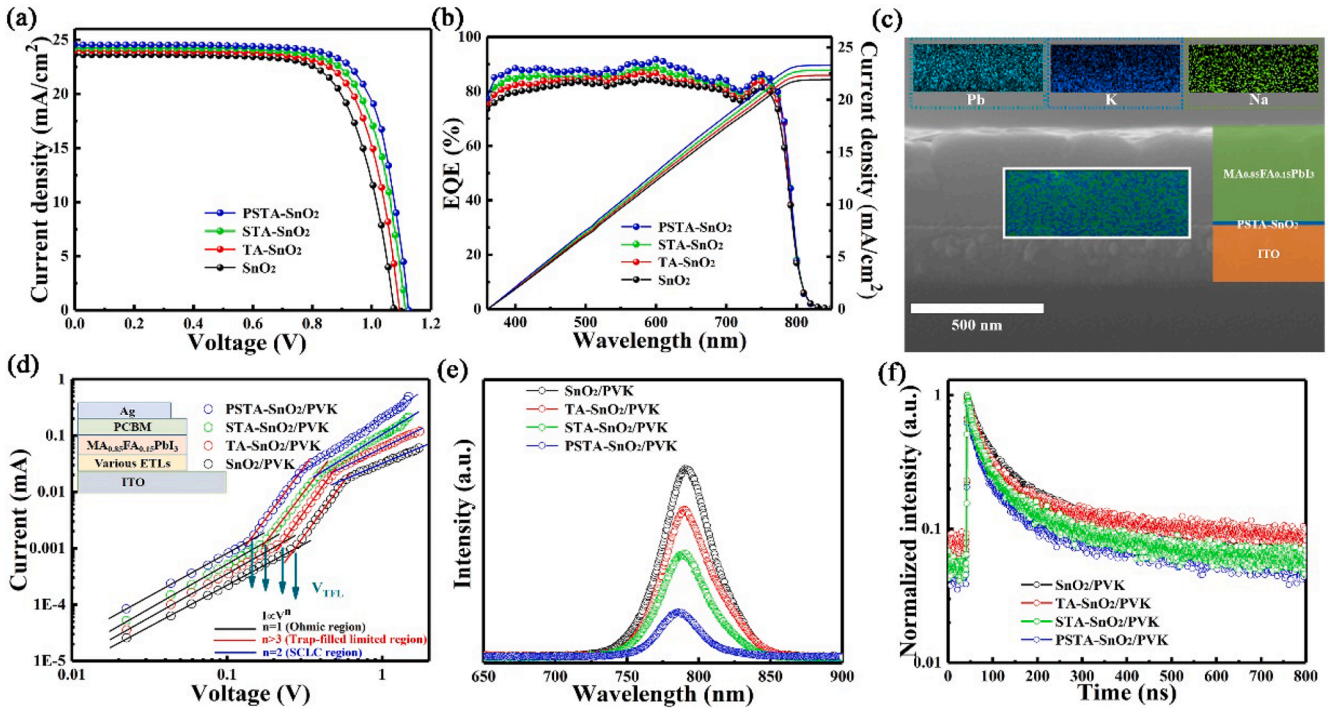

Fig. 4. (a) J-V characteristics of PSCs based on SnO_2, TA-SnO_2, STA-SnO_2 and PSTA-SnO_2 ETLs under reverse scan under standard AM 1.5 illumination (100 mW cm^{-2}). (b) EQE and the integrated J curves for corresponding devices. (c) Elemental mapping images through the cross-section of ITO/PSTA-SnO_2/perovskite film. (d) Dark J-V characteristics measurements with electron-only device structure of ITO/various ETLs/$MA_{0.85}FA_{0.15}PbI_3$/PCBM/Ag. (e) Steady-state PL spectra and (f) TRPL spectra decay of perovskite films deposited on SnO_2, TA-SnO_2, STA-SnO_2 and PSTA-SnO_2 ETLs.

results indicate the obtained perovskite films exhibit higher crystal quality and flatter morphology, which facilitates improved interfacial charge transfer and achieves high PV performance of PSCs.

The current density–voltage (J-V) curves of $MA_{0.85}FA_{0.15}PbI_3$ PSCs based on different ETLs are shown in Fig. 4a, and the corresponding PV parameters are summarized in Table 1 and Table S4. The optimized PCEs of PSCs based on SnO_2, TA-SnO_2, STA-SnO_2 and PSTA-SnO_2 ETLs measured in reverse scan are 18.25%, 19.37%, 20.38% and 21.14%, respectively. The external quantum efficiency (EQE) spectra of all PSCs measured from 360 nm to 850 nm and corresponding integrated current density curves are shown in Fig. 4b. Obviously, the spectral responses of PSCs based on SnO_2, TA-SnO_2, STA-SnO_2 and PSTA-SnO_2 ETLs exhibit a progressively enhanced tendency in the entire wavelength range, and the integrated J_{sc} is 21.99, 22.38, 22.84 and 23.27 mA/cm^2, respectively, exhibiting a good agreement with J-V results. Furthermore, the nearly hysteresis-free forward and reverse sweep curves of these modulated SnO_2-based PSCs can be observed in Fig. S12. The hysteresis index (HI) calculated by HI = ($PCE_{reverse}$ - $PCE_{forward}$)/$PCE_{reverse}$ are 0.075, 0.048, 0.026 and 0.024 for SnO_2, TA-SnO_2, STA-SnO_2 and PSTA-SnO_2-based devices, respectively [48], indicating the hysteresis behavior has been strongly suppressed.

As previously reported, both enhancement of PCE and suppression of hysteresis behavior are generally associated with the defects passivation in all functional layers of devices and the enhanced charge transport capability [49–51]. Therefore, based on the above analysis, on one hand, the improved device performance in our case can be ascribed to the improved electrical properties of ETLs, especially the reduction of non-radiative recombination centers of oxygen vacancy caused by the chelating reactions, which greatly facilitates the electron transport and collection. On the other hand, the improved crystal quality and morphology of perovskite films deposited on these ETLs are also key factors for realizing high-performance PSCs with suppressed hysteresis.

However, let's pay back attention to the XRD patterns in Fig. S11. We find although the diffraction intensity of the STA-SnO_2 and PSTA-SnO_2 based perovskite films gradually increases compared to that in TA-SnO_2 based one, the increase amplitude is too small to bring about such huge enhancement of PCE and great suppression of hysteresis. Therefore, there might be another important factor that contributes to it. After analyzing the additives, it is worth noting the K^+ and Na^+ ions in STA and PSTA additives. During the annealing process, a portion of them might diffuse from ETLs into perovskite films. To verify the occurrence of such diffusion, the EDX mapping images of cross-sectional SEM image with the structure of ITO/PSTA-SnO_2/perovskite film is shown in Fig. 4c to more visually observe the spatial distribution of these elements. The uniform spatial distribution of Pb element in perovskite film indicates the formation of dense and uniform perovskite structure. Moreover, both the apparent existence of Na and K signals and the distribution over the entire test range indicate these ions indeed diffuse into perovskite films and exist within perovskite films. The XPS survey spectra of perovskite films deposited on these ETLs and the core-level spectra of Na 1 s, K 2p and Sn 3d are presented as well to further demonstrate above discussion. As shown in Fig. S13, we confirm that K+ and Na+ ions are indeed present at the surface of PSTA- and STA-SnO_2 based perovskite films. These K^+ and Na^+ ions can occupy the surface defect states and grain boundaries to passivate negatively charged defects through ionic interactions and inhibit ion migration [52]. Moreover, the Na^+ ions also apt to be absorbed into MA vacancies due to its similar size relative to MA^+, which also realizes the effective passivation of defects at perovskite film [30]. As a result, the defects in perovskite films depositing on the STA-SnO_2 and PSTA-SnO_2 ETLs are further reduced, which is another important reason for the enhancement in PCE.

Table 1
The main PV parameters of $MA_{0.85}FA_{0.15}PbI_3$ based PSCs based on SnO_2, TA-SnO_2, STA-SnO_2 and PSTA-SnO_2 ETLs.

ETL	Scan direction	V_{oc} (V)	J_{sc} (mA/cm^2)	FF (%)	PCE (%)
SnO_2	Reverse	1.08	23.52	71.85	18.25
	Forward	1.06	23.07	68.93	16.89
TA-SnO_2	Reverse	1.10	24.01	73.35	19.37
	Forward	1.08	23.55	72.49	18.44
STA-SnO_2	Reverse	1.11	24.27	75.66	20.38
	Forward	1.10	23.90	75.21	19.86
PSTA-SnO_2	Reverse	1.12	24.47	76.87	21.14
	Forward	1.12	24.13	76.56	20.64

To quantitatively evaluate the defects in these perovskite films, Fig. 4d shows the dark J-V curves of pure electron-only devices with the structure of glass/ITO/ETL/$MA_{0.85}FA_{0.15}PbI_3$/PCBM/Ag to extract the variations of trap state density (n_{trap}) of these perovskite films. All curves consist of three regions: the linear ohmic response region at low bias, the trap-free space-charge-limited current (SCLC) region and the trap-filling regime. The electron mobility (μ_e) of these ETLs can be evaluated from the SCLC region by Mott–Gurney law [53]:

$$J_D = 9\varepsilon_0\varepsilon_r\mu_e V^2/8L^3$$

where ε_r (32) is the relative dielectric constant of perovskite, ε_0 (8.8542 × 10^{-14} F/cm) is the vacuum permittivity, e (1.602 × 10^{-19} C) is elementary charge of the electron and L (500 nm) is the thickness of perovskite film. We can find that μ_e gradually increases for perovskite film deposited on SnO_2, TA-SnO_2, STA-SnO_2 and PSTA-SnO_2 ETLs. Moreover, the trap density (n_{trap}) of all perovskite films can be determined by the formula [54]:

$$n_{trap} = 2\varepsilon_0\varepsilon_r V_{TFL}/(eL^2)$$

where V_{TFL} is the onset voltage of the trap-filled limit region and e is the electron charge. The n_{trap} gradually decreases for SnO_2, TA-SnO_2, STA-SnO_2 and PSTA-SnO_2-based devices due to the decrease of corresponding V_{TFL}. These results are in good agreement with the variation tend of J-V curves, implying that introducing these additives indeed gradually improve the crystal quality of $MA_{0.85}FA_{0.15}PbI_3$ films by passivating the defects.

Another important factor affecting the PV performance of PSCs is charge transfer kinetics. The steady-state photoluminescence (PL) spectra of perovskite films deposited on these ETLs are shown in Fig. 4e. The emission intensities of perovskite films deposited on modulated SnO_2 ETLs show more remarkable quenching effect compared to that of SnO_2/perovskite sample, implying the efficient electron transport and extraction from perovskite layer [55]. Moreover, the blue shift of emission peaks also indicates a decrease in defect states at the ETL/perovskite interface and at the perovskite grain boundaries, which is also consistent with above analysis results [56]. Time-resolved photoluminescence (TRPL) curves of corresponding samples are presented in Fig. 4f. All spectra can be well fitted by a bi-exponent decay function of I = A_1 exp ($-t/\tau_1$) + A_2 exp ($-t/\tau_2$). Detailed fitting parameters are summarized in Table S5. The yielded average lifetimes can be determined to be 59.8, 46.5, 39.0 and 32.7 ns for perovskite films deposited on SnO_2, TA-SnO_2, STA-SnO_2 and PSTA-SnO_2 ETL, respectively. Such reduction trend further testifies the beneficial effects of modulated SnO_2 ETLs on promoting efficient electron transport and suppressing non-radiative recombination.

To elucidate the changes in charge transport process within these PSCs devices, the electrochemical impedance spectroscopy (EIS) measurements are further carried out under dark condition. The Nyquist plots of the PSCs as well as the equivalent circuit model are shown in Fig. 5a, and the corresponding fitting parameters including series resistance (Rs), transfer resistance (Rtr), and recombination resistance (Rrec) are listed in Table S6. Wherein, the Rs mainly reflects the electron transport capability. The Rtr and Rrec are associated with the charge transfer and recombination process in devices, respectively. Notably, the smaller Rs and Rtr values but larger Rrec values have been obtained in modulated SnO_2-based devices compared to those in control one, which further testifies the improved charge transport efficiency and suppressed

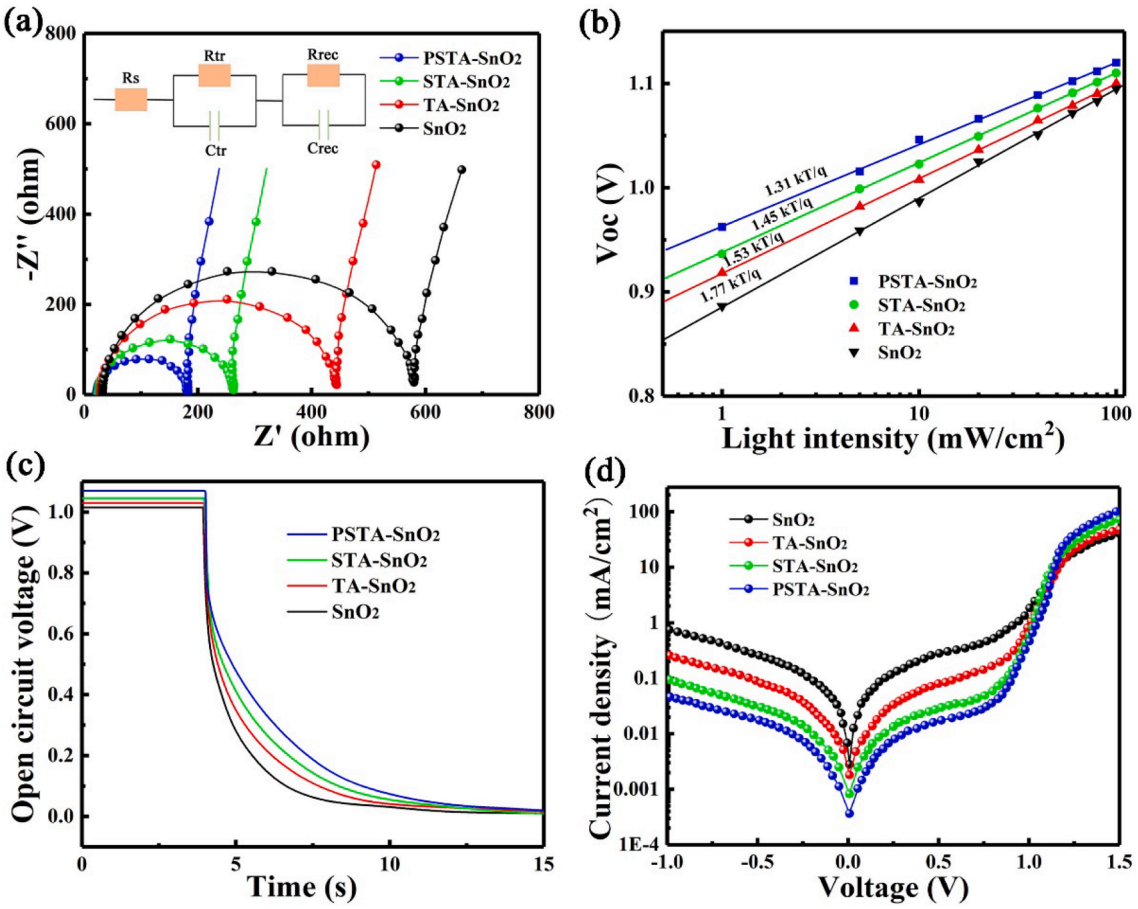

Fig. 5. (a) Nyquist plots of PSCs based on SnO_2, TA-SnO_2, STA-SnO_2 and PSTA-SnO_2 ETLs in the frequency range of 1 MHz to 0.01 kHz under 0 V bias voltages. (b) Open-circuit voltage dependence on light intensity of PSCs based on SnO_2, TA-SnO_2, STA-SnO_2 and PSTA-SnO_2 ETLs. (c) The OCVD curves of the PSCs based on SnO_2, TA-SnO_2, STA-SnO_2 and PSTA-SnO_2 ETLs. (d) J-V curves of PSCs with different ETLs measured under the dark condition plotted with a semi-log scale.

recombination process in these modulated devices.

Light intensity-dependent Voc measurements and open-circuit voltage decay (OCVD) measurements are other important techniques for characterizing charge carrier recombination rate in PSCs devices. Fig. 5b shows the light intensity-dependent Voc curves, where the slope of Voc against the logarithm of light intensity satisfies the following relationship [57]:

$$Voc = nkTln(I)/q$$

where n represents the ideal coefficient associated with recombination, k is the Boltzmann constant, T is the temperature, I is the light intensity and q is the elemental charge. The smaller value of the slope, the lower level of Shockley-Read-Hall (SRH) recombination [58-60]. The slope of PSCs based on SnO_2, TA-SnO_2, STA-SnO_2 and PSTA-SnO_2 ETLs decreases from 1.77 to 1.53, 1.45 and 1.31 kT/q, respectively, indicating trap-assisted non-radiative recombination at the ETL/perovskite interface gets effectively suppressed. Fig. 5c gives the open-circuit voltage decay (OCVD) curves. All modulated SnO_2-based PSCs exhibit higher initial values of Voc and slower decay rate compared to control device, validating the realization of suppressed recombination process and prolonged the lifetime of the carriers [61]. The dark J-V curves are also shown in Fig. 5d. The progressive reduction of leakage currents of PSCs with TA-SnO_2, STA-SnO_2 and PSTA-SnO_2 as ETLs compared to control devices also indicates the suppression of non-radiative recombination within these devices. All of the above analyses about perovskite films and devices proves the additives indeed play a great role in improving the quality of ETL, optimizing interface property and reducing defects across devices.

The degree of energy band matching at the interface between ETL and perovskite films also determines the kinetic of charge extraction and recombination. To gain insights into the effects of additives on the interfacial band alignment, ultraviolet photoelectron spectroscopy (UPS) and ultraviolet visible (UV–vis) absorption spectra are adopted to determine the work function (WF), valence band maximum (VBM), conduction band minimum (CBM) and the bandgaps of these ETLs and perovskite films. As presented in Fig. 6a and b and Fig. S14, all ETLs and perovskite films exhibit similar absorption spectra and the bandgap energy can be determined to be 3.83 eV and 1.56 eV from the Tauc curves, respectively. The UPS spectra of SnO_2, TA-SnO_2, STA-SnO_2, PSTA-SnO_2 ETLs and corresponding perovskite films depositing on them are shown in Fig. 6c-l and Fig. S15. The corresponding E_F values are determined to be −4.31, −4.28, −4.25, −4.25 and −4.16 eV, respectively, and the valence band maximum (VBM) values are 3.67, 3.66, 3.65, 3.63 and 1.4 eV lower than E_F, respectively [62–64]. Accordingly, the schematic diagram of device structures deposited on various ETLs, the diffusion behavior of alkali metal ions, and the energy band diagrams are illustrated in Fig. 7a and b to more intuitively demonstrate the band alignment between these ETLs and perovskite films. Apparently, these additives successfully turned the conduction band of SnO_2 ETLs and gradually became more compatible with that of the perovskite layer, which is another key factor in facilitating the electron extraction and transport [65,66].

The reproducibility and stability are the crucial properties for the future development of PSCs. Therefore, we prepared 20 pieces devices for each PSCs, and the improved PV parameters and narrow distribution of additive-modulated SnO_2 based PSCs shown in Fig. S16 indicate such

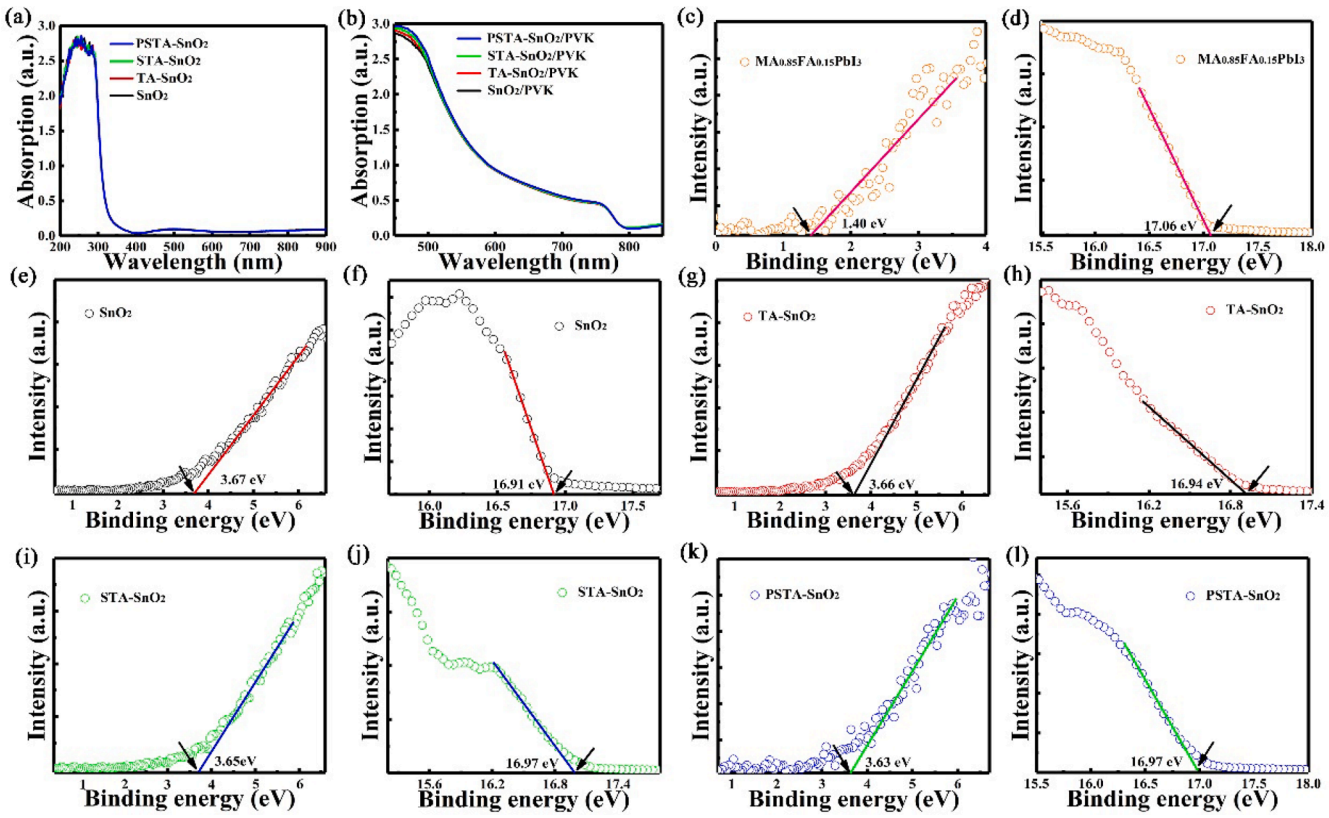

Fig. 6. (a) The UV–vis absorption spectra of SnO_2, TA-SnO_2, STA-SnO_2 and PSTA-SnO_2 ETLs. (b) The UV–vis absorption spectra of $MA_{0.85}FA_{0.15}PbI_3$ films deposited on different ETLs. (c), (e), (g), (i) and (k) show the secondary electron cut-off region of ultraviolet photoelectron spectroscopy (UPS) spectra of $MA_{0.85}FA_{0.15}PbI_3$ film, SnO_2, TA-SnO_2, STA-SnO_2 and PSTA-SnO_2 ETLs. (d), (f), (h) and (j) illustrate the valence band region of UPS spectra of $Ma_{0.85}F_{0.15}I_3$ film, SnO_2, TA-SnO_2, STA-SnO_2 and PSTA-SnO_2 ETLs.

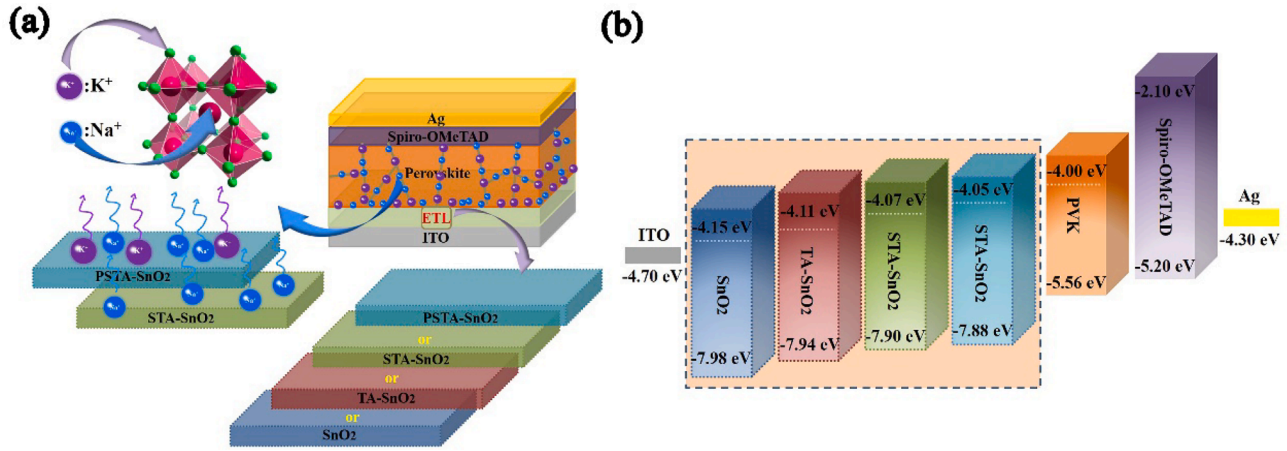

Fig. 7. (a) The left part is the diffusion diagram of K^+ and Na^+ ions from SnO_2, TA-SnO_2, STA-SnO_2 and PSTA-SnO_2 ETLs to perovskite film, the right part is device structure with additive chemical structure of TA, STA and PSTA, respectively. (b) The energy band diagram of PSCs based on SnO_2, TA-SnO_2, STA-SnO_2 and PSTA-SnO_2 ETLs.

strategy is beneficial for fabricating high-efficient PSCs with good reproducibility. The steady-state PCE measurements are carried out to evaluate the effects of above optimization on the long-term performance of PSCs, as shown in Fig. 8a. All champion devices were measured at the maximum power point (MPP) (0.86 V for SnO_2, 0.88 V for TA-SnO_2, 0.90 V for STA-SnO_2 and 0.91 V for PSTA-SnO_2 based devices) under AM 1.5G illumination. The initial output PCE of SnO_2, TA-SnO_2, STA-SnO_2 and PSTA-SnO_2 based PSCs are 17.67%, 18.42%, 19.56%, and 20.44%, respectively. After 150 s of continuous illumination, the corresponding PCE are reduced to 95.5%, 97.2%, 98.1% and 98.6% of initial value, respectively, indicating the improved stability of PSCs based on additive modulated SnO_2 ETLs. We also test the long-term stability of these devices. As shown in Fig. 8b, all devices were stored for 60 days at an ambient condition with temperature of 25 °C and a relative humidity (RH) of 45%. The retarded decay curves indicate the usage of TA, STA and PSTA can effectively improve the stability of PSCs.

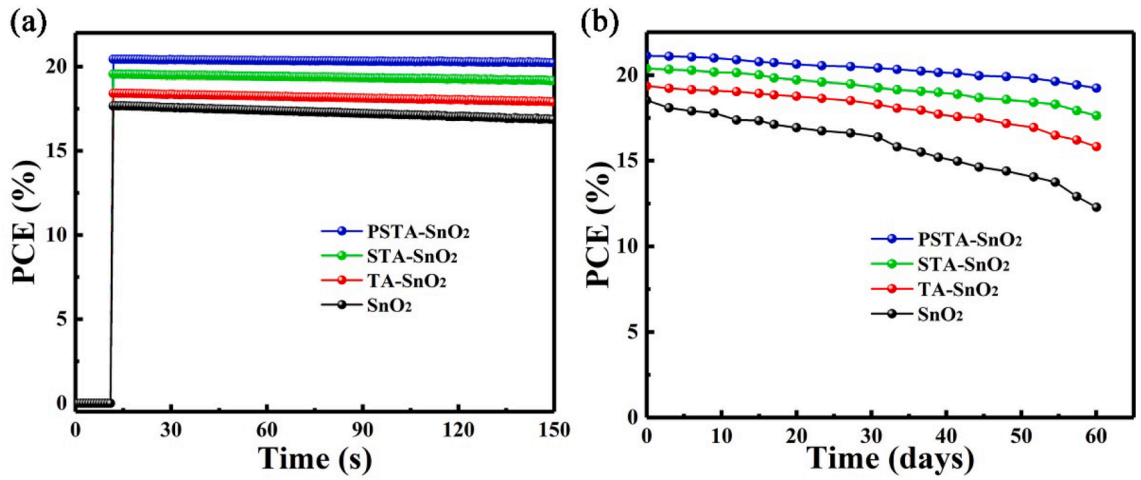

Fig. 8. (a) Stabilized PCE measurements based on SnO_2, TA-SnO_2, STA-SnO_2 and PSTA-SnO_2 ETLs at constant voltages of 0.86 V, 0.88 V, 0.90 V and 0.91 V, respectively. (b) Long term stability measurement under air condition for PSCs based on SnO_2, TA-SnO_2, STA-SnO_2 and PSTA-SnO_2 ETLs.

4. Conclusion

In summary, we proposed a facile and effective method to comprehensively enhance the PV performance of PSCs by modulating SnO_2 ETLs with chelating agents containing movable alkali metal cations of STA and PSTA. Amazingly synchronous defect passivation for entire PSCs devices has been achieved. In detail, the chelating function of additives improves the agglomerative nature of SnO_2 nanocrystals and leads to the formation of pinhole-free and uniform ETLs with reduced vacancy defects, which improves the electrical conductivity and electron mobility to facilitate the extraction and transport of charge carriers. Moreover, the K^+ and Na^+ ions diffused into perovskite from STA-SnO_2 and PSTA-SnO_2 ETLs efficiently passivate the defects on the surface and grain boundaries of perovskite films, so that both interface of perovskite/ETL and crystal quality of perovskite films are simultaneously optimized, which can further accelerate the charge transfer, effectively suppress the hysteresis behavior induced by ion migration and improve the long-term stability of devices. As a result, we achieved an optimal PCE of 21.14% and 20.38% in $MA_{0.85}FA_{0.15}PbI_3$ PSCs based on PSTA-SnO_2 and STA-SnO_2 ETLs with nearly hysteresis-free and enhanced stability, respectively. Such strategy of synchronous defect passivation can be easily integrated into the large-scale manufacturing techniques such as inkjet printing, doctor-blade coating, screen printing and roll-to-roll deposition with low cost, which shows great potential for prompting the development of practical application of efficient and stable planar PSCs.

Declaration of Competing Interest

The authors declare that they have no known competing financial interests or personal relationships that could have appeared to influence the work reported in this paper.

Acknowledgements

The authors would like to acknowledge financial support for this work from National Nature Science Foundation of China (Grant Nos. 61775081, 22075101, 61904066, 11904127, and 61475063), Program for the development of Science and Technology of Jilin province (Item No. 20200801032GH, 20190103039JH, 20190103002JH and 20180414008GH), the Thirteenth Five-Year Program for Science and Technology of Education Department of Jilin Province (Item No. JJKH20190998KJ, JJKH20190994KJ, JJKH20191021KJ, JJKH20191022KJ, JJKH20191019KJ, JJKH20190550KJ), and Construction Program for Innovation Research Team of Jilin Normal University (Grant No.201703).

Appendix A. Supplementary data

Supplementary data to this article can be found online at https://doi.org/10.1016/j.cej.2020.127387.

References

[1] https://www.nrel.gov/pv/assets/pdfs/cell-pv-eff-emergingpv.20200919.pdf.
[2] A. Kojima, K. Teshima, Y. Shirai, T. Miyasaka, J. Am. Chem. Soc. 131 (2009) 6050–6051.
[3] J.-Y. Seo, H.-S. Kim, S. Akin, M. Stojanovic, E. Simon, M. Fleischer, A. Hagfeldt, S. M. Zakeeruddin, M. Grätzel, Energy Environ. Sci. 11 (2018) 2985–2992.
[4] N.J. Jeon, H. Na, E.H. Jung, T.Y. Yang, Y.G. Lee, G. Kim, H.W. Shin, S.I. Seok, J. Lee, J. Seo, Nat. Energy 3 (2018) 682–689.
[5] F. Wang, M. Yang, Y. Zhang, L. Yang, L. Fan, S. Lv, X. Liu, D. Han, J. Yang, Adv. Sci. 6 (2019) 1801170.
[6] W. Tress, N. Marinova, T. Moehl, S.M. Zakeeruddin, M.K. Nazeeruddin, M. Grätzel, Energy Environ. Sci. 8 (2015) 995–1004.
[7] J.K. Kim, S.U. Chai, Y. Ji, B. Levy-Wendt, S.H. Kim, Y. Yi, T.F. Heinz, J.K. Nørskov, J.H. Park, X. Zheng, Adv. Energy Mater. 8 (2018) 1801717.
[8] S. Yang, J. Dai, Z. Yu, Y. Shao, Y. Zhou, X. Xiao, X.C. Zeng, J. Huang, J. Am. Chem. Soc. 141 (2019) 5781–5787.
[9] D.H. Kang, N.G. Park, Adv. Mater. 31 (2019) 1805214.
[10] C.L. Davies, M.R. Filip, J.B. Patel, T.W. Crothers, C. Verdi, A.D. Wright, R.L. Milot, F. Giustino, M.B. Johnston, L.M. Herz, Nat. Commun. 9 (2018) 293.
[11] Z. Liu, B. Sun, X. Liu, J. Han, H. Ye, Y. Tu, C. Chen, T. Shi, Z. Tang, G. Liao, J. Mater. Chem. A 6 (2018) 7409–7419.
[12] H. Zhao, S. Wang, M. Sun, F. Zhang, X. Li, Y. Xiao, J. Mater. Chem. A 6 (2018) 10825–10834.
[13] Q. Jiang, L. Zhang, H. Wang, X. Yang, J. Meng, H. Liu, Z. Yin, J. Wu, X. Zhang, J. You, Nat. Energy 2 (2016) 16177.
[14] Q. Jiang, Z. Chu, P. Wang, X. Yang, H. Liu, Y. Wang, Z. Yin, J. Wu, X. Zhang, J. You, Adv. Mater. 29 (2017) 1703852.
[15] F. Gao, Y. Zhao, X. Zhang, J. You, Adv. Energy Mater. 10 (2019) 1902650.
[16] Y. Bai, X. Meng, S. Yang, Adv. Energy Mater. 8 (2018) 1701883.
[17] Q. Wang, Q. Dong, T. Li, A. Gruverman, J. Huang, Adv. Mater. 28 (2016) 6734–6739.
[18] H. Tan, A. Jain, O. Voznyy, X. Lan, F.P. García de Arqer, J.Z. Fan, R. Quintero-Bermudez, M. Yuan, B. Zhang, Y. Zhao, F. Fan, P. Li, L.N. Quan, Y. Zhao, Z.-H. Lu, Z. Yang, S. Hoohland, E.H. Sargent, Science 355 (2017) 722–726.
[19] L. Zuo, Z. Gu, T. Ye, W. Fu, G. Wu, H. Chen, J. Am. Chem. Soc. 137 (2015) 2674–2679.
[20] Y. Dong, W. Li, X. Zhang, Q. Xu, Q. Liu, C. Li, Z. Bo, Small. 12 (2016) 1098–1104.
[21] L. Yang, Y. Gao, Y. Wu, X. Xue, F. Wang, Y. Sui, Y. Sun, M. Wei, X. Liu, H. Liu, ACS Appl. Mater. Interfaces 11 (2019) 792–801.
[22] K. Domanski, E.A. Alharbi, A. Hagfeldt, M. Grätzel, W. Tress, Nat. Energy. 3 (2018) 61–67.
[23] D. Yang, R. Yang, K. Wang, C. Wu, X. Zhu, J. Feng, X. Ren, G. Fang, S. Priya, S. Liu, Nat Commun. 9 (2018) 3239.
[24] J.M. Azpiroz, E. Mosconi, J. Bisquert, F. De Angelis, Energy Environ. Sci. 8 (2015) 2118–2127.
[25] X. Zheng, B. Chen, J. Dai, Y. Fang, Y. Bai, Y. Lin, H. Wei, X. Zeng, J. Huang, Nat. Energy 2 (2017) 17102.

[26] C. Bi, Y. Shao, Y. Yuan, Z. Xiao, C. Wang, Y. Gao, J. Huang, J. Mater. Chem. A 2 (2014) 18508–18514.
[27] M. Jiang, J. Yuan, G. Cao, J. Tian, Chem. Eng. J. 402 (2020), 126152.
[28] F. Huang, P. Siffalovic, B. Li, S. Yang, L. Zhang, P. Nadazdy, G. Cao, J. Tian, Chem. Eng. J. 394 (2020), 124959.
[29] B. Chen, P.N. Rudd, S. Yang, Y. Yuan, J. Huang, Chem. Soc. Rev. 48 (2019) 3842–3867.
[30] D.-Y. Son, S.-G. Kim, J.-Y. Seo, S.-H. Lee, H. Shin, D. Lee, N.-G. Park, J. Am. Chem. Soc. 140 (2018) 1358–1364.
[31] Y. Shao, Z. Xiao, C. Bi, Y. Yuan, J. Huang, Nat. Commun. 5 (2014) 5784.
[32] P. Qin, T. Wu, Z. Wang, X. Zheng, X. Yu, G. Fang, G. Li, Solar RRL. 3 (2019) 1900134.
[33] P. Qin, G. Yang, Z. Ren, S. Cheung, S. So, L. Chen, J. Hao, J. Hou, G. Li, Adv. Mater. 30 (2018) 1706126.
[34] W. Ke, G. Fang, Q. Liu, L. Xiong, P. Qin, H. Tao, J. Wang, H. Lei, B. Li, J. Wan, G. Yang, Y. Yan, J. Am. Chem. Soc. 137 (2015) 6730–6733.
[35] J. Chen, X. Zhao, S.-G. Kim, N.-G. Park, Adv. Mater. 31 (2019) 1902902.
[36] S. Yang, J. Yao, Y. Quan, M. Hu, R. Su, M. Gao, D. Han, J. Yang, Light Sci. Appl. 9 (2020) 117.
[37] R.S. Katiyar, P. Dawson, M.M. Hargreave, G.R. Wilkinson, J. Phys. C: Solid State Physics 4 (1971) 2421–2431.
[38] R.N. Mariammal, K. Ramachandran, B. Renganathan, D. Sastikumar, Sensor. Actuat. B-Chem. 169 (2012) 199–207.
[39] B. Cheng, J.M. Russell, W.S. Shi, L. Zhang, E.T. Samulski, J. Am. Chem. Soc. 19 (2004) 5972–5973.
[40] J. Xu, Y. Li, H. Huang, Y. Zhu, Z. Wang, Z. Xie, X. Wang, D. Chen, G. Shen, J. Mater. Chem. 21 (2011) 19086–19092.
[41] H. Zhou, Q. Chen, G. Li, S. Luo, T.-B. Song, H.-S. Duan, Z. Hong, J. You, Y. Liu, Y. Yang, Science 345 (2014) 542–546.
[42] J. Chen, N.G. Park, Adv. Mater. 31 (2018) 1803019.
[43] F. Wang, Y. Zhang, M. Yang, L. Fan, L. Yang, Y. Sui, J. Yang, X. Zhang, Nano Energy 60 (2019) 198–204.
[44] A. A. Zhumekenov, V. M. Burlakov, M. I. Saidaminov, A. Alofi, M. A. Haque, B. Turedi, B. Davaasuren, I. Dursun, N. Cho, A. M. EI-Zohry, M. D. Bastiani, A. Giugni, B. Torre, E. D. Fabrizio, O. F. Mohammed, A. Rothenberger, T. Wu, A. Goriely, O. M. Bakr, ACS Energy Lett. 2 (2017) 1782–1788.
[45] Z. Pang, Y. Sun, Y. Gao, X. Zhang, Y. Sun, J. Yang, F. Wang, L. Yang, J. Power Sources. 438 (2019), 226957.
[46] N.J. Jeon, J.H. Noh, W.S. Yang, Y.C. Kim, S. Ryu, J. Seo, S.I. Seok, Nature 517 (2015) 476–480.
[47] Q. Chen, H. Zhou, T.-B, Song, S. Luo, Z. Hong, H.-S, Duan, L. Dou, Y. Liu, Y. Yang, Nano Lett. 14 (2014) 4158–4163.
[48] D. Bi, C. Yi, J. Luo, J.-D. Décoppet, F. Zhang, Shaik M. Zakeeruddin, X. Li, A. Hagfeldt, M. Grätzel, Nat. Energy. 1 (2016) 16142.
[49] P. Chen, Y. Bai, S. Wang, M. Lyu, J.-H. Yun, L. Wang, Adv. Funct. Mater. 28 (2018) 1706923.
[50] Y. Yuan, J. Huang, Acc. Chem. Res. 49 (2016) 286–293.
[51] B. Wu, K. Fu, N. Yantara, G. Xing, S. Sun, T.C. Sum, N. Mathews, Adv. Energy Mater. 5 (2015) 1500829.
[52] N. Li, S. Tao, Y. Chen, X. Niu, C.K. Onwudinanti, C. Hu, Z. Qiu, Z. Xu, G. Zheng, L. Wang, Y. Zhang, L. Li, H. Liu, Y. Lun, J. Hong, X. Wang, Y. Liu, H. Xie, Y. Gao, Y. Bai, S. Yang, G. Brocks, Q. Chen, H. Zhou, Nat. Energy. 4 (2019) 408–415.
[53] Z.B. Wang, M.G. Helander, M.T. Greiner, J. Qiu, Z.H. Lu, Phys. Rev. B 80 (2009), 235325.
[54] D. Shi, V. Adinolfi, R. Comin, M. Yuan, E. Alarousu, A. Buin, Y. Chen, S. Hoogland, A. Rothenberger, K. Katsiev, Y. Losovyj, X. Zhang, P.A. Dowben, O.F. Mohammed, E.H. Sargent, O.M. Bakr, Science 347 (2015) 519–522.
[55] Y.Q. Zhou, B.S. Wu, G.H. Lin, Z. Xing, S.H. Li, L.L. Deng, D.C. Chen, D.Q. Yun, S. Y. Xie, Adv. Energy Mater. 8 (2018) 1800399.
[56] J.-Y. Seo, R. Uchida, H.-S. Kim, Y. Saygili, J. Luo, C. Moore, J. Kerrod, A. Wagstaff, M. Eklund, R. McIntyre, N. Pellet, S.M. Zakeeruddin, A. Hagfeldt, M. Grätzel, Adv. Funct. Mater. 28 (2018) 1705763.
[57] X. Zhang, C.W. Pinion, J.D. Christesen, C.J. Flynn, T.A. Celano, J.F. Cahoon, J. Phys. Chem. Lett. 4 (2013) 2002–2009.
[58] H. Zhang, X. Ren, X. Chen, J. Mao, J. Cheng, Y. Zhao, Y. Liu, J. Milic, W.-J. Yin, M. Grätzel, W.C.H. Choy, Energy Environ. Sci. 11 (2018) 2253–2262.
[59] M. Kuik, L.J.A. Koster, G.A.H. Wetzelaer, P.W.M. Blom, Phys. Rev. Lett. 107 (2011), 256805.
[60] D. Yang, X. Zhou, R. Yang, Z. Yang, W. Yu, X. Wang, C. Li, S. Liu, R.P.H. Chang, Energy Environ. Sci. 9 (2016) 3071–3078.
[61] M. Qin, J. Ma, W. Ke, P. Qin, H. Lei, H. Tao, X. Zheng, L. Xiong, Q. Liu, Z. Chen, J. Lu, G. Yang, G. Fang, A.C.S. Appl, Mater. Interfaces. 8 (2016) 8460–8466.
[62] P. Qin, G. Fang, W. Ke, F. Cheng, Q. Zheng, J. Wan, H. Lei, X. Zhao, J. Mater. Chem. A 2 (2017) 2742–2756.
[63] P. Qin, H. Lei, X. Zhao, Q. Liu, H. Tao, G. Yang, W. Ke, L. Xiong, M. Qin, X. Zhao, G. Fang, Adv. Mater. Interfaces. 3 (2016) 1500799.
[64] P. Qin, Q. He, C. Chen, X. Zheng, G. Yang, H. Tao, L. Xiong, L. Xiong, G. Li, G. Fang, Solar RRL 1 (2017) 1700058.
[65] J. Shi, X. Xu, D. Li, Q. Meng, Small 11 (2015) 2472–2486.
[66] X. Ge, X. Qu, L. He, Y. Sun, X. Guan, Z. Pang, C. Wang, L. Yang, F. Wang, F. Rosei, J. Mater. Chem. A 7 (2019) 27225–27235.